CPP

Contributions to Plasma Physics

www.cpp-journal.org

Editors
W. Ebeling
G. Fußmann
T. Klinger
K.-H. Spatschek

Coordinating Editors
M. Dewitz
C. Wilke

WILEY-VCH

REPRINT

Contrib. Plasma Phys. **49**, No. 7-8, 455 – 466 (2009) / **DOI** 10.1002/ctpp.200910045

Spallative Ablation of Metals and Dielectrics

N.A. Inogamov * [1], **A.Ya. Faenov**[2,3], **V.A. Khokhlov**[1], **V.V. Zhakhovskii**[2,4], **Yu.V. Petrov**[1], **I.Yu. Skobelev**[2], **K. Nishihara**[4], **Y. Kato**[5,3], **M. Tanaka**[3], **T.A. Pikuz**[2,3], **M. Kishimoto**[3], **M. Ishino**[3], **M. Nishikino**[3], **Y. Fukuda**[3], **S.V. Bulanov**[3], **T. Kawachi**[3], **S.I. Anisimov**[1], and **V.E. Fortov**[2]

[1] Landau Institute for Theoretical Physics, Russian Academy of Sciences, Chernogolovka 142432, Russia
[2] Joint Institute for High Temperatures, Russian Academy of Sciences, Moscow 125412, Russia
[3] Kansai Photon Science Institute, Japan Atomic Energy Agency, Kyoto 619-0215, Japan
[4] Institute of Laser Engineering, Osaka University, Osaka 565-0871, Japan
[5] The Graduate School for the Creation of New Photonics Industries, Hamamatsu, Shizuoka 431-1202, Japan

Received 30 April 2009, accepted 03 June 2009
Published online 08 October 2009

Key words X-ray ablation of dielectrics, warm dense matter, spallative ablation.
PACS 42.55.Vc; 79.20.Ds; 52.35.Tc

The results of theoretical and experimental studies of ablation of LiF crystal by X-ray beam having photons with $89.3\,\mathrm{eV}$ and very short duration of pulse $\tau = 7$ ps are presented. It is found that the crater is formed for fluences above the threshold $F_{abl} \approx 10\,\mathrm{mJ/cm^2}$. Such a small threshold is one order of magnitude less than the one obtained for X-ray ablation by longer (nanoseconds) pulses. The theory explains this dramatic difference as a transition from more energy-consuming evaporative ablation to spallative ablation, when the pulse duration decreases from ns to ps time ranges. Previously, the spallative mechanism of ablation was exclusively attributed to removal of target materials of metal and semiconductor by the short laser pulses with optical photons $\sim 1\mathrm{eV}$. We demonstrate that tensile stress created in dielectrics by short X-ray pulse can produce spallative ablation of target even for drastically small X-ray fluences.

© 2009 WILEY-VCH Verlag GmbH & Co. KGaA, Weinheim

1 Introduction

Rapid development of short duration X-ray lasers with the use of high order harmonic generation by femtosecond laser pulses [1], or with transient-collisional scheme [2], or, particularly, with oscillations of free relativistic electron beam (X-ray free electron laser, XFEL) [3, 4] stimulates studies of surface damage in different materials. The advancement of X-ray laser (XRL) technology has created feasible opportunities for fundamental investigations of materials in warm dense matter state [5] and for technological breakthrough in surface laser nano-machining [6]. The laser ablation of dielectrics has already been studied [7] over the last decades for lasers with different wavelengths and pulse durations, yet no research on X-ray ablation of dielectrics has been done. In this article we present, firstly, theoretical investigations of ablation mechanism in the case of soft XRL and dielectrics and, secondly, experimental measurements of ablation threshold for LiF crystals irradiated by short pulse of Ag XRL.

Laser-matter interaction is controlled by parameters of laser and irradiated substance. The three main substance classes are metals, semiconductors, and dielectrics. The laser parameters are photon energy $\hbar\omega$, pulse duration τ, and light intensity I, where intensity is related with energy fluence as $F = \int I dt$. Besides the above parameters, the pulse contrast also becomes significant for high intensity irradiation of condensed targets, because the pulse precursor can produce plasma, which shields condensed phase of a target during the main intense pulse. In our study, the precursor fluence is significantly below the melting threshold.

There are four basic mechanisms of laser ablation: (a) photochemical and thermal desorption, (b) surface evaporation, (c) thermomechanical or spallative ablation, and (d) dense plasma outflow from heated layer. For the last mechanism there is no sharp interface separating vapor and condensed matter, as opposed to mechanism (b). In the paper, we limit ourselves to chemically simple substance LiF and consider spallative ablation.

---

* Corresponding author: e-mail: nailinogamov@googlemail.com, Phone: +07 495 425 8767, Fax: +07 495 702 9317

© 2009 WILEY-VCH Verlag GmbH & Co. KGaA, Weinheim

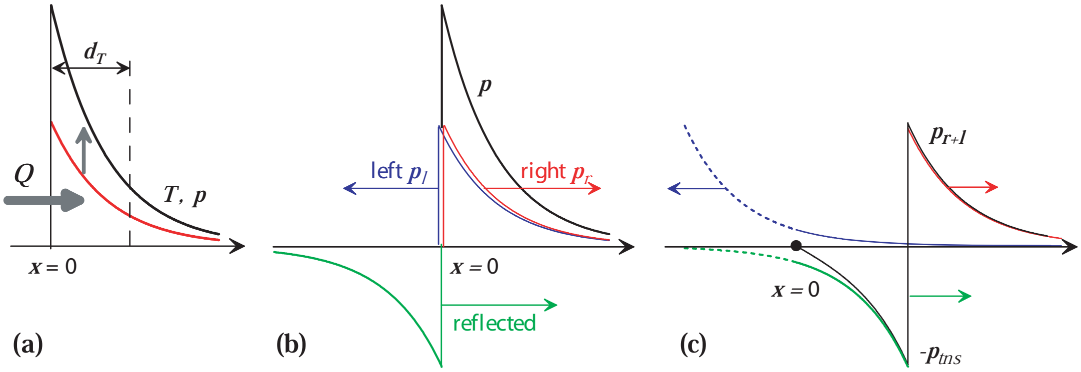

Fig. 1 (a) Growth of temperature T and pressure p (vertical arrow) during fast laser heating (energy source Q). The point $x = 0$ is the initial position of the vacuum boundary. (b) Reflection of the left wave produces the reflected wave. (c) The current pressure profile is composed from the three waves (right, left, and reflected). (Online colour:www.cpp-journal.org)

Spallative ablation is connected with (i) thermomechanical effect and (ii) cohesive property of condensed matter, which holds together. This type of ablation results from an acoustic relaxation of mechanically loaded substance. It takes place near boundary of a target when there is a space for a volume expansion of a heated layer, e.g., target borders vacuum. To load target substance, the duration τ of a laser pulse should be shorter or similar to the acoustic relaxation time $t_s = d_T/c_s$, where d_T is the heated depth in a semi-infinite target and c_s is speed of sound. Then sonic waves have no time to escape the heated surface layer during the pulse. In this case, volume expansion of a target taking time $\sim t_s$ is not fast enough to follow laser heating. This causes pressure to rise until its maximal value. This rise is called a *loading* of matter.

In metals and semiconductors irradiated with infrared or visible laser light typical values are: $c_s = 2 - 7$ km/s (e.g., Al: 5-6.5 km/s; Au: 2 km/s), $d_T = 10 - 250$ nm (Si: 10 nm; GaAs and Al: 100 nm; Au: 250 nm), $t_s = 2\,(\text{Si}) - 100\,(\text{Au})$ ps.

Acoustic decay of the pressurized layer results in creation of negative pressure $p_{neg} = -p_{tns}$ due to reflection of a sonic wave from a vacuum boundary. Appearance of a tensile stress p_{tns} is connected to attractive part of an interatomic potential U_{int} and corresponding cohesion of condensed atoms - this is impossible in gas (when only repulsive part of U_{int} is present). Cohesion allows condensed matter to resist stretching through the creation of a tensile stress. Combination of the acoustic concept with the inertia-spring idea [8] simply explains the fast acceleration of the vacuum boundary, its slow deceleration, and the finite mass of spallative layer torn from the target.

Fast speedup appears due to decay of pressure step at boundary with atomic size thickness of a boundary. Therefore, the speedup takes an atomic time $\sim$ ps $\sim a/c_s$ if duration τ is shorter than $\sim a/c_s$, where a is an interatomic distance. Duration of the deceleration $(\sim t_s = d_T/c_s)$ is defined by the pressure decreasing distance $\sim d_T$ shown in Fig.1(a). Mass inertia is a key item during acceleration and deceleration. The spallative regime of ablation is also called "inertial confinement" or "stress confinement". During acceleration, pressure difference between vacuum and a heated layer is significant. While during deceleration pressure difference between loaded matter in a heated layer and the bulk of a target becomes significant. There is no tensile stress and deceleration present if whole bulk target is homogeneously loaded: $d_f = \infty, d_T = \infty$, where d_f is a foil thickness. In this case expansion of loaded substance at a frontal boundary has form of a self-similar rarefaction wave in which pressure drops from positive value to zero. In the case of thin foils $d_T >> d_f$ initial pressure difference between positive pressure in the interior of a foil and vacuum outside accelerates frontal and rear-side boundaries, while later the same difference (but now the interior pressure is negative) decelerates these boundaries.

Thermal and mechanical processes taking place during spallative ablation are shown in Fig.1. These processes are present in all case of spallative ablation from IR to X-ray lasers and from metals/semiconductors to dielectrics. Laser absorption (the thick arrow Q) increases temperature T in the heated layer d_T. As a result of the high opacity of matter the energy is absorbed in a surface layer. If the heating time is shorter or comparable with sonic time t_s then the T growth increases pressure in the layer $\sim d_T$ thick.

© 2009 WILEY-VCH Verlag GmbH & Co. KGaA, Weinheim

Later, the pressure profile p splits into two waves: one propagates to the right side, while the other propagates to the left. This follows from D'Alembert's solution of the wave equation $p_{tt} - c_s^2 p_{xx} = 0$. The amplitudes of the right and left waves are equal because substance was at rest before an action of a laser pulse. Vacuum boundary at $x = 0$ reflects the left wave. After reflection, the total pressure profile is composed of three waves: left, right and reflected. The amplitude of the sum p_{r+l} of the right (p_r) and the left (p_l) waves shown in Fig.1(c) is $p_{r+l} \approx p/2$, where p is the maximum amplitude created during a heating stage. In linear acoustics, used here for qualitative explanations, the amplitude of the negative pressure p_{tns} in Fig.1 gradually grows up from $p_{tns}(t = -0) = 0$ in Fig.1(b) through transient values $p_{tns}(+0 < t < \infty) < p/2$ shown in Fig.1(c) to the asymptote $p/2$ with $t \to \infty$. Here we suppose that the pressure profile decays at infinity $x = \infty$ (no waves coming from the right side). For the spatially restricted pressure profile the asymptote $p/2$ is achieved for a finite time.

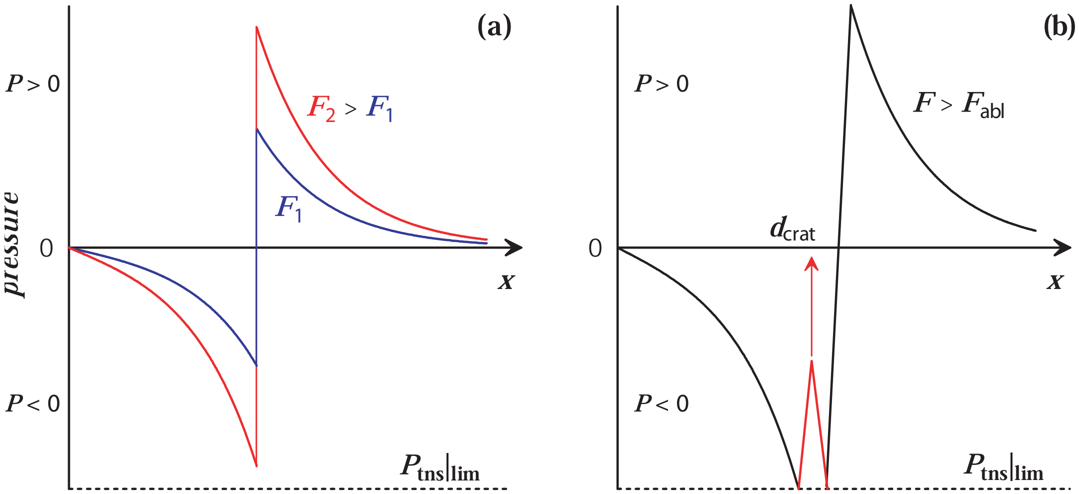

Fig. 2 (a) Growth of positive and negative pressures with fluence F. The dotted line marks the limiting strength of material $p_{tns}|_{lim}$. The amplitude of negative pressure for F_2 is smaller than $p_{tns}|_{lim}$. Therefore the fluence F_2 is smaller than spallative ablation threshold F_{abl}. (b) Beginning of spallation slightly above the threshold F_{abl}. The largest absolute value of negative pressure at a fixed instant t increases with time t. This increasing is shown in Fig.1(c). When this value achieves the limiting strength then nucleation starts and spallation begins. Due to nucleation a sharp peak at pressure profile appears and grows up to the zero value $(p \approx 0)$. The peak is marked by vertical arrow. The distance between the nucleation point marked by the arrow and the vacuum boundary defines thickness d_{spall} of a spallative plate. Near ablation threshold this thickness equals to the crater depth d_{crat} . (Online colour:www.cpp-journal.org)

The asymptote in time of value $p_{tns} = p(F)/2$ is proportional to absorbed fluence F and grows with F. This dependence is demonstrated in Fig.2 by comparison of pressure profiles obtained for different fluences F_1 and F_2. Resistance of condensed matter against stretching is limited. The limiting stress $p_{tns}|_{lim}$ shown in Fig.2 is called "tensile strength of material." Void nucleation begins at some depth d_{crat} under vacuum surface when a function $p_{tns}(F)$ overcomes $p_{tns}|_{lim}$. This condition defines a sharp threshold F_{abl} of spallative ablation. Near threshold we have $d_{crat} \sim d_T$. Above threshold a layer of thickness d_{crat} loses its connection with the target and runs away from the target after a sonic transient stage considered below. The spallated layer has a finite thickness near threshold because the stress field $p_{tns}(x, t)$ always equals to zero at vacuum boundary and increases into bulk of a target as shown in Fig.1.

Near threshold, the transient stage in metals and semiconductors is surprisingly long [9]. This is a result of the stretching ability of the liquid phase, because in metals and semiconductors nucleation takes place in melt. In contrast to this, simulations presented below show that stretched LiF nucleates in solid state near threshold. This indicates that LiF is less stretchable, which is why there are no foam and long threads connecting spallative layer and target. Comparison of nucleation in solid versus liquid has been discussed in [10, 11].

In this paper a short review of spallative ablation for the case of infrared and visible lasers acting on metals and semiconductors is given (Section 2). Section 3 presents experimental investigations of ablation of LiF targets irradiated by Ag soft X-ray laser (photon energy 89.3 eV) with small pulse duration $\tau = 7$ picosecond. An

© 2009 WILEY-VCH Verlag GmbH & Co. KGaA, Weinheim

attenuation depth d_T is 28 nm [12]. Therefore, $\tau \sim t_s$. In our case, it was found that the ablation threshold is extremely low: F_{abl} is only 10 mJ/cm ^{2}. E.g., it is an order of magnitude lower than ablation threshold for X-ray laser with long $\tau = 1.7$ nanosecond [13] pulse.

Sections 4 and 5 are devoted to new findings concerning spallative ablation in case of X-ray lasers and dielectrics. This part of the paper presents a physical model describing: (i) absorption of X-ray photons and primary ionization, (ii) relaxation of primary ions through Auger recombination, ionization by free electrons, and three body recombination, (iii) cooling of free electrons through a process of energy transfer to heavy particles, (iv) increase of pressure, generation of acoustic waves, their reflection from vacuum boundary, and creation of tensile stress.

A theoretical model with a new (for X-rays and dielectrics) assumption about spallative nature of ablation, allows us to explain the low threshold value found in our experiments.

2 Spallative ablation of metals and semiconductors

Discovery of spallative ablation begins with a surprising fact found in outstanding experiments [14] initially designed to define changes in reflectivity $R(t)$ initiated by laser heating. It was found that the function $R(t, r)$ is non-monotonous - it oscillates in time and also oscillates as function of radius r of a laser spot. These oscillations have a form of Newton rings. The rings appear after irradiation of targets by short $\hbar\omega \sim 1$ eV laser pulse with $F \sim 1$ J/cm ^{2} This pulse is called the pump pulse in the pump-probe technique of measurements. The rings were observed after the delay of order of nanosecond from the pump arrival to the target surface. The target has been illuminated after the pump by a short probe pulse, which allowed us to see an image of the Newton rings. The number of rings increases with duration of delay. Appearance of the rings is a transient phenomenon - the rings are not presented in the final picture obtained by probe delayed for a long time $(\gg 1$ ns) relative to the pump.

It turns out that the phenomenon is universal - it was found in all (many examples [14]) observed metals and semiconductors without any exceptions. But despite many attempts with similar lasers $\hbar\omega \sim 1$ eV the phenomenon with rings has never been seen in case of dielectrics. Below the explanation is given. It emphasizes the special nature of dielectrics. The reason for the ring phenomenon has been described in [15], see also [16] and references given therein. This description introduces the spallative mechanism outlined in Figs.1 and 2 into the list of the most important ablation mechanisms.

It should be emphasized that here we discuss spallative *ablation* - this is the material removal from the irradiated side. The irradiated side is the frontal side of a target. In case of foils, there is also back-side surface. Spallation at a back-side caused by a laser generated shock, is a more habitual phenomenon [10, 17–21]. We call it simply spallation.

Let's compare the influence of this effect for different lasers and materials. In the simplest case, absorption Q, given in Fig.1(a), directly forms temperature profile proportional to the local absorbed energy $\int dtQ(x,t)$ – absorption d_{abs} and heating d_T depths are equal. Below, we will see that this is the case of short duration X-ray lasers and dielectrics when $d_{abs} \approx d_T$. Lengths d_{abs} and d_T equals by reason of, firstly, an electrostatic localization of ionized electrons near their ions; secondly, a small heat conductivity resulting in weak thermal diffusion during acoustic relaxation stage. If $\tau \le t_s$ then tensile stress shown in Figs.1 and 2 appears. Negative pressures and limiting strength define threshold fluence F_{abs} separating evaporation and thermomechanical ablations.

In metals $d_{abs} \sim \delta_{skin}$ is less than d_T as a result of strong electron heat conduction κ_e acting during two-temperature stage [22], where $\delta_{skin} \sim 10 - 20$ nm is a skin depth. Therefore the sonic duration $t_s \propto d_T$ is defined by the two-temperature relaxation and not by d_{abs}. At fixed F_{abs} the two-temperature effects become weaker as duration τ grows.

A gap Δ in an energy spectrum differs metals versus semiconductors and dielectrics. The linear absorption length d_{abs}^{lin} in materials with a gap is usually much larger than a skin depth δ_{skin} in metals. Energy density F_{ob}/d_{abs}^{lin} is small in comparison with density of cohesion energy $n_{at}\varepsilon_{coh}$ if F_{ob} is an optical breakdown threshold, here n_{at} is concentration of atoms in condensed state, ε is energy per particle. Light propagation through material with a gap causes ionization - appearance of free electrons in a conduction band above a gap. Appearance of conductivity electrons increases absorption and decreases the length d_{abs}. For photons with

© 2009 WILEY-VCH Verlag GmbH & Co. KGaA, Weinheim

$\hbar\omega \sim 1$ eV electron critical density n_{cr} necessary to reflect the light is $\sim 1\%$ of atomic concentration n_{at}. If intensity I and duration τ of a laser pulse is large enough to overcome n_{cr} during the pulse action, then an instant local absorption length d_{abs} decreases down to values comparable with δ_{skin} for metals. This causes an optical breakdown as a result of a sharp growth $\propto 1/d_{abs}$ of power density (J/cm^3) transferred from laser to matter.

In dielectrics a gap Δ is significantly wider than in semiconductors while cohesion energies ε_{coh} are similar. Therefore the ratio $n_{cr}\Delta/(n_{at}\varepsilon_{coh})$ is larger for dielectrics. This means that near threshold F_{ob} dielectrics are hotter than semiconductors. It is also important that melting transfers semiconductors into metallic state. Melting heat is low against ε_{coh}. In metallic liquid state of semiconductors established after melting d_{abs} decreases to low values $\sim \delta_{skin}$ for metals. From these two circumstances (wide gap and small melting latent heat) it follows that in case of a short laser pulse $\tau < t_s$ near threshold F_{ob} the ratio of forces $p_{tns}|_{lim}/p$ is less for dielectrics, while for ablation fast load and cohesion sticking both is necessary. Dielectrics are hotter than semiconductors and their sticking near F_{ob} is weaker. Therefore spallative ablation in the case of dielectrics should be either absent, or confined to a narrow strip near $F_{ob}(\tau)$ at the F, τ plane. Let us add that in the case of the spallative ablation the ejecta composition is different from the compositions for evaporation and gas-plasma outflow.

Three classes have been presented above: (i) $d_{abs} \approx d_T$, (ii) $d_{abs} < d_T$ (metals), and (iii) the class when local d_{abs} is a function of time t_p passed from the beginning of a laser pulse. This function depends on accumulation time t_p and energy accumulated locally during t_p. This is the case of infrared or optical lasers $\hbar\omega \sim 1$ eV acting on materials with a gap $\Delta \sim \hbar\omega$ or larger than $\hbar\omega$.

In this paper the case of hard $(\hbar\omega \gg \Delta)$ photons and a short pulse acting on dielectrics is considered. It corresponds to the class (i). Critical density n_{cr} is two orders of magnitude larger than the solid state concentration n_{at} therefore it is unattainable for our 90 eV photons. — Decreasing of d_{abs} however is not necessary for increasing of energy density because the linear attenuation depth d_{abs}^{lin} is small. Consequently, even at a relatively small F the energy density F/d_{abs} may be appreciable part of cohesion energy. Evaporation needs more energy, therefore for short pulses $\tau < t_s$ the spallative ablation dominates above evaporation if $F > F_{abl}$.

3 Experimental set up and results

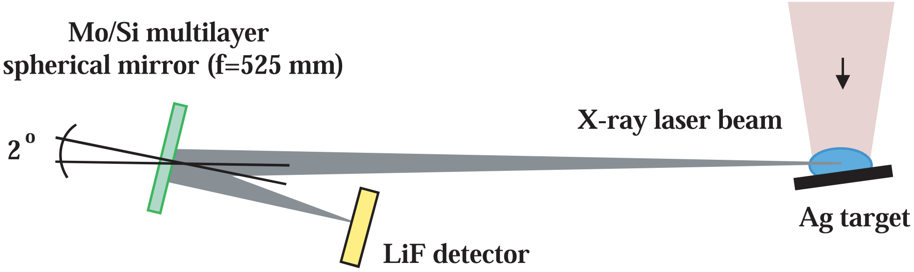

Fig. 3 Experimental set up for recording the Ag XRL beam patterns near the best focus position on a surface of a LiF crystal.

The experiment has been performed with the XRL facility at JAEA Kansai Photon Science Institute [23, 24]. The X-ray laser beam had energy $\sim 1\ \mu$J. Its horizontal and vertical divergences are 12 mrad $\times$ 5 mrad. The beam was focused on a LiF crystal of 2 mm thickness and 20 mm diameter, by using a spherical Mo/Si multi-layer mirror of 1050 mm radius of curvature shown in Fig.3. The total energy on the LiF crystal of the XRL beam, after passing 200 nm Zr filter and reflecting from the focusing mirror, was ~ 170nJ in a single shot. The luminescence of stable color centers (CCs) [25–27] formed by XRL radiation was used to measure the intensity distribution in the XRL laser focal spot [24]. After irradiation of the LiF crystal with the XRL, the photo-luminescence patterns from the CCs in LiF were observed by using a confocal fluorescence laser microscope (OLYMPUS model FV300). Also, we have used an OLYMPUS BX60 microscope in visible differential mode and an atomic force microscope (AFM, TOPOMETRIX Explorer), operated in the tapping mode, for measurements of the size of ablative spot. Large aberrations and broad scattering of the XRL beam are perceptibly seen in images in Fig.4. They could be caused mostly by the insufficient quality of Mo/Si multilayer mirror used in this experiment. The mirror has been severely contaminated with plasma debris after prolonged use in various experiments. Due to

© 2009 WILEY-VCH Verlag GmbH & Co. KGaA, Weinheim

this circumstance, as it was shown in our experiments [24], only about 6% of full laser energy is concentrated to the best focus spot of $\sim 200\,\mu\,\mathrm{m}^2$. Energy and intensity in this spot are ≈ 5 mJ/cm^2 and $\approx 7 \cdot 10^8$ W/cm^2.

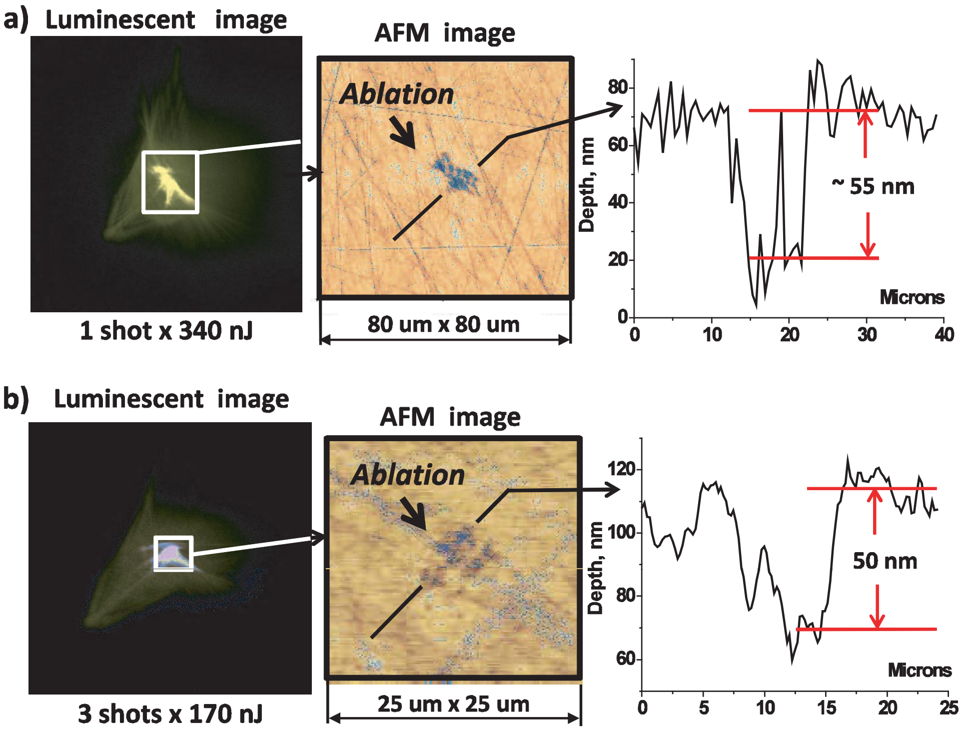

Fig. 4 (a) The 40^x magnified luminescent image and the image and trace of XRL ablative spot, measured by the AFM. They are obtained after single XRL pulse action onto a LiF crystal. The XRL fluence is 10.2 mJ/cm^2, and intensity is $1.46 \cdot 10^9$ W/cm^2. (b) The same as in (a), but obtained after action of three 3 XRL pulses. The XRL fluence of each pulse is 5 mJ/cm^2, intensity is $0.7 \cdot 10^9$ W/cm^2) . (Online colour:www.cpp-journal.org)

Two types of experimental investigations of XRL ablation threshold of LiF crystals were done. In the first experiments, Zr filter has been removed and XRL beam expanded freely and then was focused on the surface of LiF crystal. In Fig.4(a) the luminescence and AFM images of XRL beam focal spot are presented. They were obtained in a single laser shot. The laser was focused on the surface of LiF crystal after free propagation (without Zr filter) of the XRL beam. Ablation of crystal is clearly seen from AFM image and trace. The energy of the XRL beam is 350 nJ in the first experiment. Therefore the XRL laser energy threshold for LiF crystal is ≈ 10.2 mJ/cm^2. The traces obtained from AFM image show that the ablation depth d_{crat} defined in Fig.2(b) varies between 30 and 55 nm. These values are close to the absorption depth $d_{abs} \approx 28$ nm in LiF for the soft X-ray wavelength 13.9 nm [12]. They agree with our theoretical depth $\approx 40 - 50$ nm shown below in Fig.7(c).

In the second type of experiments, Zr filter has been settled inside the XRL radiation beam propagation path. In this case three shots with equal fluence have been pointed to the same focusing spot as for the first set of experiments without Zr filter. These shots were well separated in time from each other. In the case of the triple shot, the ablation threshold fluence is ≈ 5 mJ/cm^2 for each individual shot in the triplet. This value is half of the threshold for the first set of experiments. We could see from Fig.4(b) that in the second case a crater, with an ablation depth of about 50 nm, appears on the surface of the crystal. This value for d_{crat} is similar to the value obtained in the first set of experiments with double intensity XRL shot. It is necessary to emphasize, that ablation is absent if we irradiate surface with only one shot with fluence 5 mJ/cm^2.

4 Physical model

Dimensions of an irradiated spot at target surface are $\sim 10 - 20$ um, while the attenuation depth is $d_{abs}(\hbar\omega = 90\ \mathrm{eV},\ \mathrm{LiF}) = 28$ nm [12]. Therefore one dimensional approximation with hydrodynamic motion along the normal to surface direction x is enough. We divide problem into two parts. In the part described in this Section, we neglect gradients ∂_x and consider spatially homogeneous geometry. This is possible since heat penetration is decaying exponentially $\propto \exp(-x/d_T)$ and distribution of thermal energy is well localized near the surface in the layer d_T. In equations written for values averaged over the layer d_T only time derivatives remain. In the next part partial differential equations in x and t are written and solved. They define generation and propagation of sonic waves and give us an amplitude of a tensile stress created by X-ray laser.

Equations for quantities in the layer d_T are

$$dn_e/dt = Q/u_{i2} + \nu_{imp} n_e - \kappa_{rec} n_e^3, \quad Q = (F/(\sqrt{\pi} d_T \tau)) \exp(-t^2/\tau^2), \tag{1}$$

$$dE_e^s/dt = Q - \dot{E}_{ea}, \quad E_e^s = n_e u_{i2} + E_e, \quad E_e = (3/2) n_e T_e, \tag{2}$$

$$C dT_{at}/dt = \dot{E}_{ea}, \quad C \approx 6 k_B n_c, \quad n_c \approx 6 \cdot 10^{22}\,\mathrm{cm}^{-3}, \quad \dot{E}_{ea} = A E_e, \tag{3}$$

where $n_e(t)$ is concentration of electrons in the conduction band, Q (1,2) presents a laser energy source, F is X-ray fluence, u_{i2} is potential energy of ion at an energy level near the bottom of the forbidden gap Δ, $\Delta \approx 14\,\mathrm{eV}$ for LiF. LiF has the widest gap between all other dielectrics. In equation (2) E_e^s is total energy of electron subsystem, E_e is thermal energy of free electrons moving with velocity v_e above the bottom of a conduction band. Total energy E_e^s is a sum of ion potential energy and kinetic energy of electrons. Without energy sources (Q) and loses $(\dot{E}_{ea})$, total electronic energy E_e^s is conserved. Estimates show that we can neglect radiative loses at acoustic relaxation time scale, see also [28]. C is condensed state heat capacity. In the range of temperatures between room and melting temperature heat capacity of LiF crystal increases from $5 k_B n_c$ to $7 k_B n_c$ [29], where k_B is Boltzmann constant, n_c is concentration of elementary cells, LiF has two atoms per one elementary cell.

Primary ions are formed by photo-ionization by 90 eV photons. Such photons produce mainly ions Li $1s2s$ and F $1s^2 2s 2p^5$ with a hole at the internal electron orbit because rotation frequencies at these orbits are closer to photon frequency [28]. Let us denote as u_{i1} potential energy of primary ions. Photo-ionization is followed by (i) ionization through electron impact, (ii) Auger processes with participation of one internal and one free electrons, and (iii) three-body recombination with two free electrons and one ion. Auger recombination with two internal electrons is impossible for Li and F. Ion composition includes many different ions and excited states. Simple energy estimates based on fluence $F = 10\,\mathrm{mJ/cm}^2$, heating depth $d_T \approx 30\,\mathrm{nm}$, and photon energy 90 eV show that the ion concentration $n_i = n_e$ is small $(n_e \sim 10^{-2} n_c)$ and that the main contribution to ion composition is connected with single charged $Z = 1$ ions. These ions mainly occupy the highest possible energy levels. This follows from estimates of Auger frequencies. Above we denote their potential energy as u_{i2}, u_{i2} is less than u_{i1} since u_{i1} and u_{i2} ions correspond to holes at internal and external orbits respectively.

The electron impact ionization frequency ν_{imp} necessary for equation (1) is taken from [30]. It is written as half of a sum of frequencies for ionization of Li and F atoms: e+Li → Li+e+e, e+F → F+e+e. Ionization potential in expressions for ν_{imp} is changed to the gap width Δ. Expressions for ν_{imp} are

$$\nu_{imp}^{Li} = \langle v_e \sigma_{imp}^{Li} \rangle n_c\,[\,\mathrm{s}^{-1}], \quad \langle v_e \sigma_{imp}^{Li} \rangle = 11 \cdot 10^{-8} \sqrt{\beta/(\beta+1)}/(\beta+1.5) e^{-\beta}\,[\,\mathrm{cm}^3/\,\mathrm{s}], \quad \beta = \Delta/T_e,$$

$$\nu_{imp}^{F} = \langle v_e \sigma_{imp}^{F} \rangle n_c, \quad \langle v_e \sigma_{imp}^{F} \rangle = 0.7 \cdot 10^{-8} \sqrt{\beta/(\beta+1)}/(\beta+0.18) e^{-\beta}$$

The term ν_{imp}^{Li} is frequency of ionization of a Li neutral by impact of an electron from a conduction band. It is proportional to concentration n_{Li}^o of Li neutrals. Concentration of ions is small $(\sim 1\%)$, therefore $n_{Li}^o \approx n_c$. LiF is an ion crystal with two sublattices of positive Li and negative F ions. We refer as atoms to these ions since Li+F pair of them has zero total charge. Our ions appear after photo-ionization by 90 eV photons, or after ionization by free electron impact. They are hole in the valent band and are positively charged Li+F pair or are individual positive ions of Li or F. The coefficients κ_{rec} of three-body recombination for Li and F have been found from condition of detailed equilibrium [30].

Laser energy is absorbed by electrons. Therefore at initial stages free electrons are hotter than heavy particles (atoms and ions). Gradually energy of electron subsystem is transferred to heavy particles through electron-atom (e-a) and electron-ion (e-i) collisions. The e-a collisions dominate because ion concentration is small.

The e-a energy transfer is rather slow process since electron-atom mass ratio is small. Energy transfer rate is $\dot{E}_{ea} = \Delta\varepsilon \nu_{ea} n_e$, where $\Delta\varepsilon \approx 3(m_e/M_{Li})((3/2)k_B T_e)$ is averaged energy transferred from electron to atom in one collision, $\nu_{ea} = \langle v_e \sigma_{ea}\rangle n_c$ is collision frequency, $v_e = \sqrt{3k_B T_e/m_e}$. Let us separate thermal energy E_e in expression for $\dot{E}_{ea}$. We have $\dot{E}_{ea} = A E_e$, where $A = 3(m_e/M_{Li})\langle v_e \sigma_{ea}\rangle n_c$. Estimates for Li atom radius varies in the range $r_{Li} = 0.15{-}0.20$nm. Then the energy exchange coefficient is $A = (10{-}20)\cdot 10^{11}\mathrm{s}^{-1}$.

The energy exchange term $\dot{E}_{ea}$ has change sign when temperatures T_e, T_a are equal. Writing $\dot{E}_{ea} = AE_e$ we neglect this effect. This is reasonable because when $T_e = T_a = T_{eq}$ the energy E_e is negligible in comparison with the energy density of atomic subsystem $(\approx CT_{eq})$ since equilibrium temperatures are low $(T_{eq} \sim 1\,\mathrm{kK})$, and concentration n_e of free electrons at these temperatures is very small. In this approximation, system (1-3) does not include T_{at} (only $\dot{T}_{at}$ is presented). Therefore equations (1) and (2) for derivatives $\dot{n}_e$ and $\dot{T}_e$ are independent from the last equation (3) for $\dot{T}_{at}$.

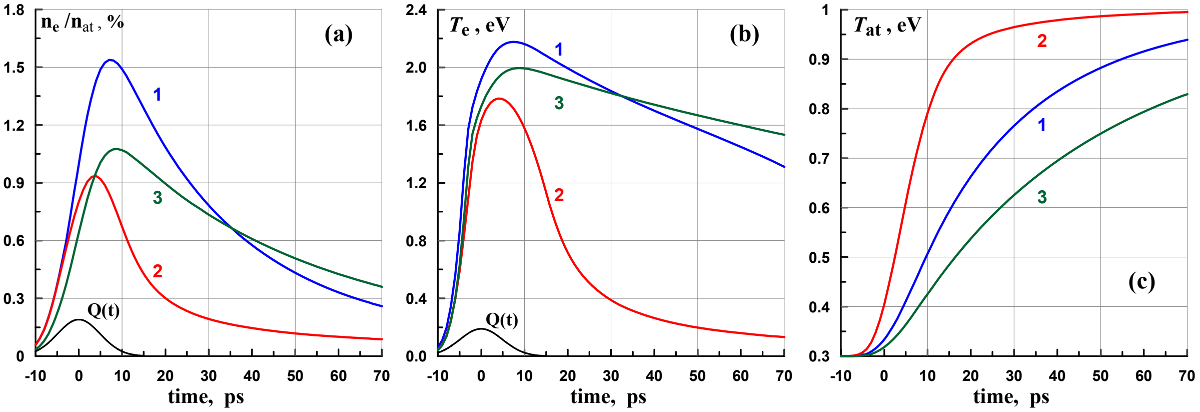

Fig. 5 (a) Concentration in % of free electron population in LiF. Growth of n_e is due to photo-ionization and decay is due to recombination. The curve $Q(t)$ gives a temporal profile of a laser source. The curves 1, 2, and 3 in (a,b,c) correspond to: the curve 1 $u_{i2} = 14$ eV, $A = 2\cdot 10^{11}$ s^{-1}; the curve 2 $u_{i2} = 14$ eV, $A = 9\cdot 10^{11}$ s^{-1}; and the curve 3 $u_{i2} = 25$ eV, $A = 2\cdot 10^{11}$ s^{-1}. (b) Temperature T_e increases and decreases. Recombination heating supports T_e against e-a cooling after the end of the laser pulse $Q(t)$. (c) Increase of atomic temperature T_{at} during acoustic relaxation time $\sim t_s \approx 5$ps is larger if the e-a energy exchange is faster. The largest A corresponds to the curves 2 in (a,b,c). Value of $A = (10-20)\cdot 10^{11}$ s^{-1} based on the size of a Li atom, which is high enough to afford significant growth of T_{at} and consequent growth of p_{at} during acoustic stage. But if A is smaller, then p_{at} and p_{tns} will be weaker. Therefore results for $A = 2\cdot 10^{11}$ s^{-1} are also presented as the curves 1 and 3.

Results of integration of system (1-3) are presented in Fig.5. Maximum concentration $n_e(t)$ is achieved near the end of the Gaussian X-ray pulse $Q(t)$, $\tau = 7$ ps, (1). Ion potential energy u_{i2} significant for the ratio between kinetic and potential contributions to total electronic energy E_e^s has been varied between the gap width Δ and the value near potentials u_{i1} of primary ions created by absorption of 90 eV photons. This has been done to see influence of electron-hole plasma composition on results. It has been found that this influence is moderate - compare dependencies 1 and 3 in Fig.5. For higher u_{i2} the potential contribution to E_e^s is larger, and the energy transfer to atoms is more slow.

The value A of the e-a energy transfer (3) is significant for results. Concentration $n_e(t)$ and electron temperature $T_e(t)$ fall down faster for larger value of A. Then $T_{at}(t)$ increases faster. Our final goal is to estimate tensile stress p_{tns} induced by X-ray pulse since this stress shown in Fig.2 drives the spallative ablation. The amplitude p_{tns} is proportional to pressure $p_{at} + p_e$ achieved in a heated layer $d_T \approx 30$ nm during acoustic relaxation time $t_s \sim 5$ps. While $p_{at}(t) \propto T_{at}(t)$ in isochoric (density is fixed) system (1)-(3). Therefore larger A means larger p_{at} at $t \sim t_s$ and larger p_{tns}.

Solutions of system (1)-(3) is valid only up to $t \sim t_s$ because this system neglects volume expansion of a heated layer d_T. Adiabatic expansion decreases the final values T_{at}^{fin} of the dependencies $T_{at}(t)$ shown in Fig.5(c). But difference in temperatures between initial room temperature state $(T = T_{rt})$ and the final state after heating $(T = T_{at}^{fin})$ is moderate. It follows that the temperature decrease $T_{at}^{fin} \to T_{at}^{expns}$ due to this expansion is small: $T_{at}^{fin} - T_{at}^{expns} \ll T_{at}^{fin}$. Indeed, the "distance" $\rho_{ini} - \rho_b(s) \ll \rho_{ini}$, $T_{isch}(s) - T_b(s) \ll T_{isch}(s)$

© 2009 WILEY-VCH Verlag GmbH & Co. KGaA, Weinheim

between the vapor-solid coexistence curve $p = p_{vap}$ (binodal) and the isochoric line $\rho = \rho_{ini} = \rho_b(T_{rt})$ is small if deviations from initial point (ρ_{ini}, T_{rt}) are moderate, because the binodal and the isochor diverge at a small angle at a phase plane (ρ, T). Here the subscripts "b", "isch," and "ini" mean a binodal (vapor-solid coexistence curve), an isochor line, and an initial room temperature state; s is entropy (matter expands adiabatically after XRL heating and electron-atom relaxation); $s(T_{isch})$ increases with increase of isochoric temperature T_{isch}; all T in this place are T_{at}; saturated vapor pressure $p_{vap} \approx 0$, $p_{vap} \ll p_{tns}$ at our temperatures. But strong difference in pressures $p_b = p_{vap} \approx 0$ and $p_{isch}(s)$ between the binodal and the isochor causes hydrodynamic expansion and stretching.

Again, $T_e(t)$ decreases faster if the coefficient A is larger. This causes faster growth of atomic temperature $T_{at}(t)$ shown in Fig.5(c) - compare the curve 2 against the curves 1 and 3. Atomic pressure p_{at} is approximately proportional to T_{at} because $p_{at} \approx \Gamma E_{at}$, $E_{at} \approx C T_{at}$, where Γ is Grueneisen parameter. This proportionality holds during acoustic stage in matter not affected by rarefaction wave propagating from vacuum boundary. Acoustic effects are considered below.

5 Acoustic stage

In our experimental conditions $(\tau \sim t_s, \tau = 7\ \text{ps}, t_s \approx 5\ \text{ps})$ laser pulse overlaps with sonic relaxation. In this case it is necessary to follow the laser heating process together with hydrodynamical motion. Equations and physical model are

$$\rho^o \frac{\partial}{\partial t}\frac{E_e}{\rho} = \frac{\rho^o}{\rho} Q - \frac{\rho^o}{\rho}\dot{E}_{ea} - p_e \frac{\partial u}{\partial x^o} + \frac{\partial}{\partial x^o}\left(\frac{\rho \kappa_e}{\rho^o}\frac{\partial T_e}{\partial x^o}\right), \quad Q = \frac{F}{\sqrt{\pi}\tau d_T}\exp\left(-\frac{t^2}{\tau^2} - \frac{x^o}{d_T}\right). \quad (4)$$

This is an electron energy E_e balance with a source Q, and loses of electron energy through atom heating, through work done by electron pressure $p_e = (2/3)E_e$ for adiabatic expansion, and electron thermal conduction loses from heated layer into cold bulk of a target. Electrons are electrostatically bound to ionized layer. Therefore we will neglect the last term. In this case the electron temperature T_e is not presented in equations and we can use energy E_e to represent current state of the electron subsystem because p_e and $\dot{E}_{ea}$ (3) depends on E_e only.

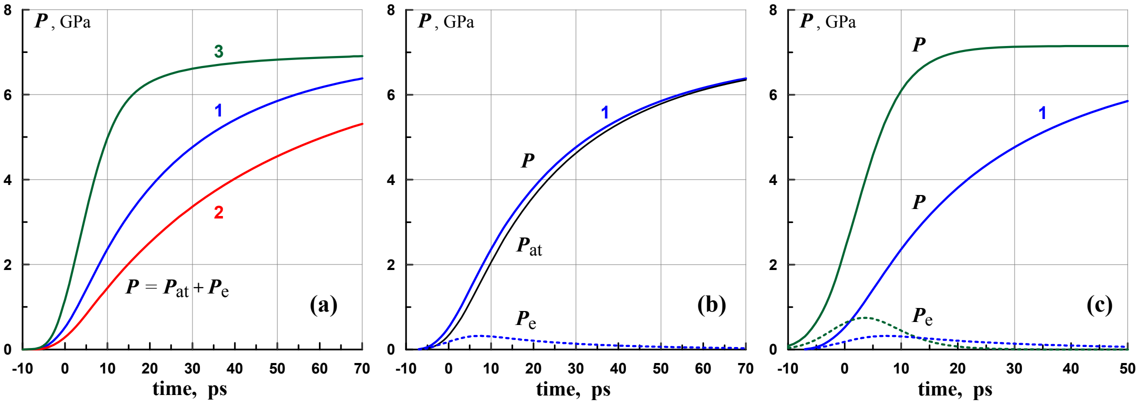

Fig. 6 (a) Dependencies of total pressure $p(t)$ on u_{i2} and A. (b) Comparison of electronic and atomic contributions to total pressure. (c) Comparison of ODE $\{n_e, T_e\}$ (1), (2) and $\{E_e\}$ -equation corresponding to system (4,5).

In (4) ρ^o is initial density. The LiF target has homogeneous density distribution before the pulse. The X-ray absorption depends on column mass. This is why the source Q (4) decays with Lagrangian coordinate x^o. Velocity is u. Mass conservation equation in Lagrangian variables is $\rho^o \partial x^o = \rho \partial x$. Dynamical equation describing acceleration or deceleration of matter under action of pressure waves is $\rho^o \partial u/\partial t = -\partial p/\partial x^o$, $p = p_e + p_{at}$. Atomic energy E_{at} balance with e-a heat transfer source and adiabatic expansion and phonon heat conduction loses is

$$\rho^o \partial(E_{at}/\rho)/\partial t = (\rho^o/\rho)\dot{E}_{ea} - p_{at}\partial u/\partial x^o + (\partial/\partial x^o)((\rho\kappa_{at}\ \rho^o)\partial T_{at}/\partial x^o). \quad (5)$$

© 2009 WILEY-VCH Verlag GmbH & Co. KGaA, Weinheim

The thermal diffusion term in (5) becomes significant only at late stages $(\sim 1\,\text{ns})$ because the coefficient $\kappa_{ea} \approx 2-4$ W/m/K is small in our range of temperatures T_{at}.

System (4), (5) (PDE - partial differential equations) differs from system (1), (2) (ODE - ordinary differential equations). The PDE include space variable x, x^o and describe sonic relaxation important to define an amplitude of a tensile stress generated by X-ray pulse. This is significant advantage over the ODE. But on the other hand the PDE simplify kinetics of energy transfer through ion subsystem to heat. The PDE do not include equation for concentration of free electrons n_e and potential energy of electron subsystem. This causes overestimation of the rate of the Q → e → a energy transfer and amplitude of pressure. To understand significance of these overestimates, let us drop out the x and ∇_x terms in PDE (4), (5). Then we obtain $\{E_e\}$-equation $\dot{E}_e = Q - AE_e$ with Q from (1).

Comparison of solutions of ODE $\{n_e, T_e\}$ (1), (2) and $\{E_e\}$-equation is shown in Fig.6(c). Indeed, the pressure increase for the $\{E_e\}$-solution is three times higher than the increase for the $\{n_e, T_e\}$-solution at the instant $t = t_s = 5\,\text{ps}$. This is the worst case with the smallest A, when the pressure growth is slow, see Fig.6(a). The difference between $\{n_e, T_e\}$ and $\{E_e\}$ pressure dependencies $p(t)$ is smaller for faster exchange.

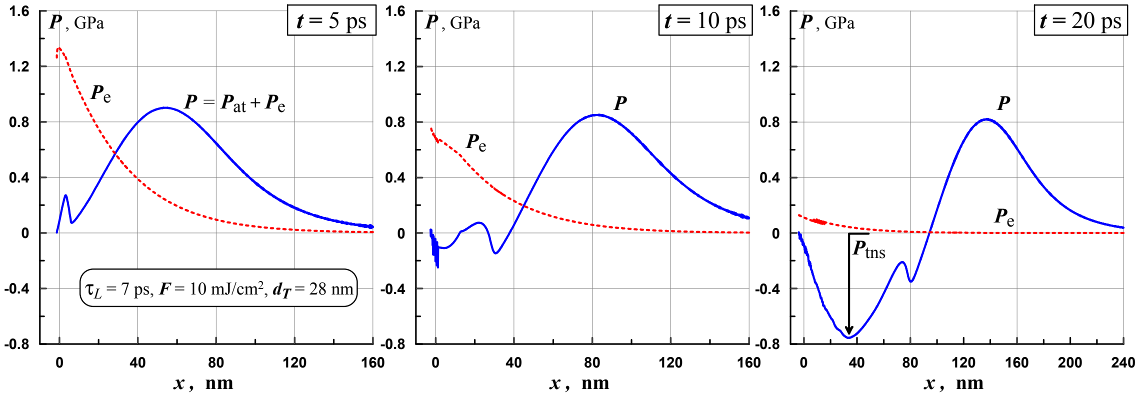

Fig. 7 Gradual formation of a tensile tail of a rarefaction wave; $F = 10\text{mJ/cm}^2$, $\tau = 7\text{ps}$, $d_T = 28\text{nm}$, $A = 2{\cdot}10^{11}\,\text{s}^{-1}$.

With this in mind, let us consider solutions of PDE (4, 5). Obvious initial conditions for equations are: $\{E_e\}$ $E_e(t=-\infty) = 0$; $\{n_e, T_e\}$ $n_e(-\infty) = 0$, $T_e(-\infty) = T_{rt} = 300\,\text{K}$; (4, 5) $n_e(x, t=-\infty) = 0$, $T_e(x, -\infty) = 300\,\text{K}$. Typical behavior is shown in Fig.7. Gradual absorption of XRL pulse rises energy density and pressure in a surface layer. Figs.7 from (a) to (c) demonstrates D'Alembert separation, reflection, and formation of negative total pressure. Pressure creation through XRL heating stage and wave separation stage overlap as a result of $\tau \sim t_s$, therefore, we do not see decrease of maximum pressure from p to $p/2$ as in the case $\tau \ll t_s$ shown in Fig.1(b). If $\tau \ll t_s$ then, first, maximum positive pressure increases during a heating stage τ from 0 to p, second, pressure decreases from p to $p/2$ at an acoustic stage t_s, and after that, third, in linear acoustics maximum pressure remains constant equal to $p/2$ during propagation of a sonic wave. In the case presented in Fig.7 maximum positive pressure monotonously grows during a time interval $\sim t_s$ and after that remains constant.

Fig.7(c) shows a final shape of an acoustic profile composed from compression $p > 0$ and tensile $p < 0$ parts just before its separation from vacuum boundary. After the separation instant $t_{sep} \approx 25\,\text{ps}$ motion of the vacuum boundary "vb" stops and its velocity v_{vb} becomes zero: $v_{vb}(t > t_{sep}) = 0$. Maximum expansion velocities are $v_{vb}(t \sim 5-10\,\text{ps}) \approx 0.2$ km/s. Without nucleation and breaking the maximum amplitude $p_{tns}(t)$ of an instant tensile stress profile increases up to the instant t_{sep}. After that it does not change. Maximum final value of p_{tns} for the case shown in Fig.7(c) is 8 kbar. This value is obtained for the slowest e-a energy transfer. As stated above, for the larger A the final value of p_{tns} is larger.

Wave amplitudes are rather small, linear acoustics works well, and therefore without nucleation final tensile amplitude is proportional to fluence F, if XRL duration τ is fixed. Acoustic transformation from beginning to separation of wave takes a relatively long time interval $t_{sep} \approx (3-4)t_s$. For $\tau \sim t_s$ or $\tau > t_s$ without nucleation final maximum value of p_{tns} is $\propto 1/\tau$ if F is fixed. E.g., the final p_{tns} is twice higher for $\tau = 3.5\,\text{ps}$ than the value shown in Fig.7(c) corresponding to $\tau = 7\,\text{ps}$.

© 2009 WILEY-VCH Verlag GmbH & Co. KGaA, Weinheim

Simulations (4,5) have been done with a wide range equation of state (EoS) for aluminum [31]. This is possible because LiF has approximately the same density (2% difference), the same cold curve $p(\rho, T = 0)$ (small difference between Al and LiF in our range of $p \sim \pm 1$ GPa), and approximately the same Grueneisen parameter as Al: $p_{at}^{Al}/E_{at}^{Al} \approx p_{at}^{LiF}/E_{at}^{LiF}$. Therefore functions $p_{at}(\rho, E_{at})$ for Al and LiF are close to each other. Comparison of Hugoniot curves $p(\rho/\rho_0),\ \Delta E(\rho/\rho_0),\ \Delta E = E - E_0$ confirms this. This means that for the same energy supply Q (4) the hydrodynamic fields $\rho(x,t),\ u(x,t),\ p(x,t),\ E_{at}(x,t),\ E_e(x,t)$ for Al and LiF are very similar. But there is some small difference connected with heat capacity, temperatures, and melting. Our system (4,5) is written in terms of energies $E_e,\ E_{at}$ - temperatures T_e and T_{at} are less significant, since we omit electron heat conductivity κ_e in (4) (quasi-neutrality and smallness of the Debye length $D_D = \sqrt{k_B T_e/4\pi n_e e^2} \ll d_T,\ D_D$ is less than 1 nm) and because of at acoustic time scale influence of atomic heat conductivity κ_{at} in (5) is negligible. Noteworthy, in this case, there is no difference between electronic subsystem of metals and dielectrics, since electronic Gruenisen parameter is the same $p_e/E_e = 2/3$ for degenerate and classical electron gases.

Heat capacity C_{LiF} of LiF (3) is approximately double the C_{Al} because cell concentrations n_c are the same and number of atoms per elementary cell is twice as high for LiF. Therefore, increments of temperatures due to heating simulated with Al EoS is approximately twice higher than it should be for LiF. As stated above this is insignificant (T_{at} does not enter equations) until there is no melting. Triple temperatures are $T_{LiF} = 1121$ K and $T_{Al} = 933$ K. Temperatures T_{at}^{Al} in simulation shown in Fig.7 are ≈ 1 kK at the left edge corresponding to vacuum boundary. Temperature increment in Al is ≈ 0.7 kK at this edge. This means that in LiF the highest T_{at}^{LiF} after heating and relaxation is near 0.7 kK. LiF remains solid for $F = 10$ mJ/cm^2. This differs LiF from metals and semiconductors having spallative ablation threshold higher than melting threshold [11, 22]. Metals and semiconductors nucleate in liquid while LiF in solid states. Thickness of Al melt in Fig.7(c) is 12 nm at a final stage when absorption and e-a energy transfer are finished. This weakly influence results for LiF, since energy spent on melting is 1.3 mJ/cm^2 - this is a small part of XRL fluence $F = 10$ mJ/cm^2.

Fig.7(a),(b) shows that up to $t \sim 10$ ps electronic and atomic pressures $p_e,\ p_{at}$ are comparable near a vacuum boundary: $p|_{vb} = p_e + p_{at} = 0$, where $p|_{vb}$ is total pressure at a vacuum boundary. At this stage hot free electrons act as an internal mechanical expander stretching LiF lattice beyond its equilibrium interatomic spacing. Equilibrium at given T_{at} corresponds to a vapor-solid coexistence curve (binodal) with $p_{at} = p_{sat\ vap} \approx 0$. Electronic pressure p_e expands lattice into two-phase region inside a binodal. Lattice becomes metastable, and, in principal, may nucleate in this stretched state. Pressure p_e slightly enlarges speed of sound $c_s = \sqrt{(\partial p/\partial \rho)_s}$ when $p_e \sim p_{at}$. For $t > 10$ ps electronic contribution gradually disappears, and in Fig.7(c) inertia, kinetic energy, and ram pressure of expanding part of a target acting against resisting to stretching cohesive force [8] creates tensile stress p_{tns}. The expanding part is the part near vacuum boundary. Its thickness is $\sim d_T$.

Even weak expansion during laser pulse action decreases amplitudes of pressure p_{at} in comparison with isochoric models $\{n_e, T_e\},\ \{E_e\}$ - compare p_{at} in Fig.6(c) and Fig.7 at equal values of A, while P_e is insensitive to weak expansion because p_{at} passes through zero at the binodal while p_e depends on internal electronic energy. Review of published data on material strength $p_{tns}|_{lim}$ of dielectrics nevertheless shows that stresses presented in Fig.7 are enough for nucleation: $p_{tns}|_{lim} = 4 - 10$ kbar for PMMA [21], $p_{tns}|_{lim}$ is few kilobars for dielectrics [32]. It is known also that excitation of electronic subsystem and appearance of free electrons in a conduction band decreases elastic constants of lattice [33, 34]; $\sim 1\%$ increase of n_e decreases elastic constants for few tens of % [34]. In our case n_e population shown in Fig.5(a) is $\sim 1\%$. Changes of elastic constants decrease strength $p_{tns}|_{lim}$. Value of $p_{tns}|_{lim}$ in our case may be also decreased as a result of X-ray radiation. At a depth $\sim d_T$ irradiation creates color centers described in Section 3. Concentration of these centers is large enough to influence the value $p_{tns}|_{lim}$. More centers - weaker crystal. Decrease of threshold F_{abl} as result of incubation of these centers (see Section 3) points to this conclusion. Below spallative ablation threshold $F < F_{abl}$ the maximum stress in simulations is achieved at a depth $\approx 40 - 50$ nm under vacuum boundary. This means that at threshold the calculated crater depth is $\approx 40 - 50$ nm. Therefore the crater depth 30-50 nm measured in our experiments described in Section 3 above is in agreement with simulations.

Acknowledgements Work of NAI, VAK, and YuVP has been supported by the RFBR grant No. 09-08-00969-a. This research has been partially supported by the Japan Ministry of Education, Science, Sports and Culture, Grant-in-Aid for

© 2009 WILEY-VCH Verlag GmbH & Co. KGaA, Weinheim

Kiban A No 20244065, Kiban B No. 21360364., by the RFBR grant No. 09-02-92482-MNKS-a, and by the RAS Presidium Program of basic researches No. 27.

References

[1] Ph. Zeitoun, G. Faivre, S. Sebbam et al. Nature, **431,** 426 (2004); M. Kando, Y. Fukuda, A.S. Pirozhkov et al. Phys. Rev. Lett., **99,** 135001 (2007); E.J. Takahashi, T. Kanai, K.L. Ishikawa et al. Phys. Rev. Lett., **101,** 253901 (2008); Y. Nomura, R. Hoerlein, P. Tzallas et al. Nature Physics, **5,** 124 (2009).

[2] J. Dunn, Y. Li, A.L. Osterheld et al. Phys. Rev. Lett., **84,** 4834 (2000); M. Tanaka, M. Nishikino, T. Kawachi et al. Opt. Lett., **28,** 1680 (2003); S. Heibuch, M. Grisham, D. Martz, J.J. Rocca. Opt. Express, **13,** 4050 (2005); Y. Wang, M.A. Larotonda, B.M. Luther et al. Phys. Rev. A, **72,** 053807 (2005).

[3] `http://www.xfel.eu/` ; `http://www.riken.jp/XFEL/eng/index.html`

[4] S. Marchesini, S. Boutet, A.E. Sakdinawat et al. Nat. Photonics, **2,** 560 (2008).

[5] F.B. Rosmej, R.W. Lee, D. Riley et al. Journal of Physics: Conference Series, **72,** 012007 (2007); U. Zastrau, C. Fortmann, R.R. Faeustlin et al. Physical Review E, **78,** 066406 (2008); E. Garcia Saiz, G. Gregori et al. Nature Physics, **4,** 940 (2008); M. Berrill, F. Brizuela, B. Langdon et al. JOSA B., **25,** 32 (2008).

[6] R. Phipps (ed.), Laser Ablation and its Applications. Springer Series in Optical Sciences **129** (2007).

[7] S.J. Henleya, G.M. Fuge, M.N.R. Ashfold. J. Appl. Phys., **97,** 023304 (2005); S. Amoruso, G. Ausanio, A.C. Barone et al. J. Phys. B: At. Mol. Opt. Phys., **38,** L329 (2005).

[8] V.V. Zhakhovskii, N.A. Inogamov, K. Nishihara. JETP Lett., **87,** 423 (2008).

[9] S.I. Anisimov, N.A. Inogamov, Yu.V. Petrov et al. Appl. Phys. A, **92,** 939 (2008).

[10] V. V. Zhakhovskii, N. A. Inogamov et al. Appl. Surf. Sci., doi:10.1016/j.apsusc.2009.04.082 (2009).

[11] A. K. Upadhyay, N. A. Inogamov, B. Rethfeld, H. M. Urbassek. Phys. Rev. B, **78,** 045437 (2008).

[12] `http://henke.lbl.gov/optical_constants/`

[13] A. Ritucci, G. Tomassetti, A. Reale et al. Optics Letters, **31,** 68 (2006).

[14] K. Sokolowski-Tinten, J. Bialkowski, A. Cavalleri et al. Phys. Rev. Lett., **81,** 224 (1998).

[15] N.A. Inogamov, Yu.V. Petrov, S.I. Anisimov et al. JETP Lett., **69,** 310 (1999).

[16] N. A. Inogamov, V. V. Zhakhovskii, S. I. Ashitkov et al. JETP, **107,** 1 (2008).

[17] V.E. Fortov, D. Batani, A.V. Kilpio et al. Laser and Particle Beams **20,** 317 (2002).

[18] S. Eliezer, E. Moshe, D. Eliezer. Laser and Particle Beams **20,** 87 (2002).

[19] J.P. Cuq-Lelandais, M. Boustie, L. Berthe et al. J. Phys. D: Appl. Phys. **42,** 065402, 2009.

[20] Li Huang, Y. Yang, Y. Wang, Z. Zheng, W. Su. J. Phys. D: Appl. Phys. **42,** 045502, 2009.

[21] V. I. Vovchenko, I. K. Krasyuk, P. P. Pashinin, A. Yu. Semenov. Specific of breaking off processes in an organic glass under high speeds of deformations. 7-th Workshop Complex Systems of Charged Particles and their Interaction with Electromagnetic Radiation. GPI, Moscow, Russia. April 15-16, 2009.

[22] N. A. Inogamov, V. V. Zhakhovskii et al. Appl. Surf. Sci., doi:10.1016/j.apsusc.2009.04.139 (2009).

[23] M. Nishikino, N. Hasegawa, T. Kawachi et al. Applied Optics, **47,** 1129 (2008).

[24] A.Ya. Faenov, Y. Kato, M. Tanaka et al. Optic Letters, **34,** 941 (2009).

[25] G. Baldacchini, S. Bollanti, F. Bonfigli et al. Rev. Sci. Instrum., **76,** 113104 (2005).

[26] A. Ustione, A. Cricenti, F. Bonfigli et al. Appl. Phys. Lett., **88,** 141107 (2006).

[27] G. Tomassetti, A. Ritucci, A. Reale et al. Europhys. Lett., **63,** 681 (2003).

[28] A.V. Lankin, I.V. Morozov, G.E. Norman, S.A. Pikuz, Jr., I.Yu. Skobelev. Phys. Rev. E, **79,** 036407 (2009).

[29] `http://webbook.nist.gov/cgi/inchi/InChI%3D1S/FH.Li/h1H%3B/q%3B%2B1/p-1`

[30] L.M. Biberman, V.S. Vorobyev, I.T. Yakubov. Kinetics of Nonequilibrium Low-Temperature Plasmas (Springer, Berlin, 1987); I.I. Sobelman, L.A. Vainshtein, E.A. Yukov. Excitation of Atoms and Broadening of Spectral Lines (Springer Series on Atoms and Plasma), Springer, April 2007.

[31] A.V. Bushman, G.I. Kanel’, A.L. Ni, V.E. Fortov. Intense dynamic loading of condensed matter, Taylor & Francis Translation, 295 p., 1993.

[32] T. Antoun, L.Seaman, D.R. Curran, G.I. Kanel et al. Spall Fracture (Springer, NY etc., 2003).

[33] V. Recoules, J. Clerouin, G. Zerah, P.M. Anglade, S. Mazevet. Phys. Rev. Lett., **96,** 055503 (2006).

[34] E.S. Zijlstra, L.L. Tatarinova, M.E. Garcia. arXiv:cond-mat/0609017 [cond-mat.other]

© 2009 WILEY-VCH Verlag GmbH & Co. KGaA, Weinheim